# Anodised Aluminium Foil Winding Axial Flux Machine for Direct-Drive Robotic Applications

Jordi Van Damme, *Student Member, IEEE*, Hendrik Vansompel, and Guillaume Crevecoeur, *Member, IEEE*

***Abstract*—There is a need for higher specific torque electric actuators in novel direct-drive robotic applications. Since the specific torque is inherently limited by material properties, designers have to look at novel materials to push the specific torque limit further. In this article, anodised aluminium foil is considered as an alternative to enamelled copper wire in a yokeless and segmented armature axial flux machine. This machine topology has a high specific torque and is particularly suited for an anodised aluminium foil winding. The DC resistance, thermal properties and eventually the specific torque of a prototype test case machine are compared for both winding materials. A 3D thermal finite element model is used to analyse the influence of the thermal interface between winding body and housing, and the influence of the cooling performance on the specific torque. To conclude, anodised aluminium foil winding offers a higher specific torque in direct-drive yokeless and segmented armature axial flux actuators where the winding body thermal resistance is dominant in the thermal path from heat source to heat sink. It is experimentally shown that for the prototype machine, the torque per kg active stator mass increases 13% through the use of anodised aluminium foil.**

***Index Terms*—Aluminium, Aluminium Oxide, Anodisation, Axial Flux, Robotics, Thermal Conductivity**

## I. Introduction

ELECTRIC machines with high specific torque (Nm/kg) are gaining interest to advance upon the development of novel (quasi-)direct-drive robotic applications [1]–[4]. The Yokeless And Segmented Armature Axial Flux Permanent Magnet Synchronous Machine (YASA AFPMSM) topology is an interesting candidate for these applications since it allows to obtain a high specific torque due to a high fill factor and the absence of a stator yoke [5], [6]. This topology was already considered for a direct-drive articulated robot in [7] and quasi-direct-drive exoskeleton actuator in [8]. However, a key challenge is that the specific torque is inherently limited by material temperature limits [9]. Therefore researcher have started to look at alternative materials to further increase the specific torque and/or power. In [10], it was shown that aluminium conductors offer an interesting alternative to copper. Already for a long time, aluminium as conductor material has been used in electric machines due to its attractive properties [10]:

- Aluminium is almost 3 times lighter than copper.
- Aluminium has a lower price volatility [11] and cost [10], [12].
- Aluminium windings enable an increased recyclability of an electric motor [10].
- The use of aluminium in electric motors has a lower impact on the environment compared to copper [13]

However, the electrical conductivity of aluminium is 37% lower than that of copper. Although this can be beneficial for high-frequency machines [14], it is often detrimental for the specific torque of low frequency machines where DC winding losses tend to dominate [15]. To overcome this issue and make aluminium a viable competitor to copper in terms of machine specific torque, researchers have relied on innovative techniques to manufacture preformed aluminium coils with round [10], [16], flat [9], [12]–[14], [17]–[20] or foil [21] conductors. Preformed coils exhibit a high fill factor and a good thermal conductivity which are both attractive features when designing high specific torque motors [19], [22]–[24]. However, existing electric motors with aluminium conductors typically use organic insulation [10], [12], [19], [21]. Despite its excellent insulating and mechanical properties, its poor thermal conductivity limits the heat transfer in the winding body [16].

In this article, the use of an anodised aluminium foil is proposed to overcome this issue. It consists of aluminium foil with an electrolytically grown aluminium oxide ($Al_2O_3$)

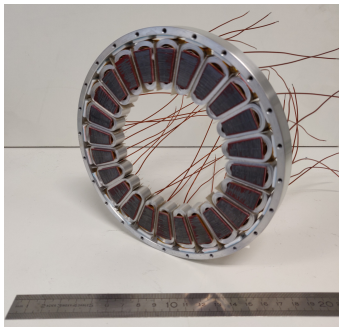

Fig. 1. Prototype axial flux machine stator with anodised aluminium foil tooth coils (before potting)

Manuscript received July 15, 2022; revised August 30, 2022; accepted October 27, 2022. J. Van Damme was awarded a Ph.D. Fellowship Strategic Basic Research (SB) from the Research Foundation Flanders (FWO) in 2019 (Grant Number: 1S87322N). The authors J. Van Damme, H. Vansompel and G. Crevecoeur are with the Department of Electromechanical, Systems and Metal Engineering, Ghent University, Ghent, 9000, Belgium, and with Flanders Make@UGent - EEDT, 3001 Leuven, Belgium. (e-mail: jordi.vandamme@UGent.be; hendrik.vansompel@UGent.be; guillaume.crevecoeur@UGent.be)

-also known as alumina- layer on both sides of the foil. In the past, anodised aluminium foil has already been used in inductors, transformers and electromagnets [25]–[27] because of its attractive features:

- Aluminium oxide has a high thermal conductivity (approximately 1.6 W/mK [28]) which allows to significantly increase the thermal conductivity of the winding body [24].
- The inorganic anodisation layer allows an operating temperature up to 500°C [26], [29].

The use of inorganic aluminium oxide insulation improves the thermal conductivity of the winding body. This was already shown experimentally for a winding material sample in [24] and in a simulation study for an automotive solenoid actuator in [30]. Moreover, a foil winding allows a high fill factor and exhibits superior thermal properties as was reported for copper foil windings in [31], [32]. Hence, both the use of aluminium oxide insulated aluminium conductors and the foil winding topology promise to improve the specific torque.

This paper aims to evaluate the specific torque of a YASA AFPMSM with anodised aluminium foil winding in comparison to an electromagnetically identical machine with enamelled copper wire. The influence of the thermal interface between winding body and housing, and the influence of the cooling performance will be studied specifically.

First, Section II motivates the need for higher specific torque motors in direct-drive robot applications and specifies the test case YASA AFPMSM that will be used throughout this comparative study. Subsequently, in Section III the winding losses are analysed and compared for both an anodised foil winding and a copper wire winding YASA AFPMSM. In Section IV, the equivalent thermal properties of a winding body are determined experimentally and compared for both winding materials. These parameters are used in 3D thermal Finite Element (FE) model of the test case YASA AFPMSM to study the influence of the thermal interface between winding body and housing on the stator thermal performance. Finally, in Section V, the specific torque of the test case YASA AFPMSM is determined experimentally for both winding materials, and the influence of the cooling performance on the specific torque is studied using the losses from Section III and the thermal model from Section IV.

## II. YASA Axial Flux PMSM for Direct-Drive Robot Applications

In novel robotic applications such as cobots, legged mobile robots, exoskeletons, and collision tolerant grippers there is the tendency to go towards (quasi-)direct drive actuators. They have a gear ratio ranging between 1:1 to 10:1 [33]. (Quasi-)Direct drive actuators inherently have a higher backdrivability which enables safer, more dexterous and dynamic robots which are capable of dealing with uncertain, unstructured and changing environments [2]–[4], [33].

Despite the attractive features offered by (quasi-)direct-drive actuators they suffer from a low specific torque caused by their low gear ratio. This limits the robot performance. For example, for an articulated robot to handle a useful payload, a system specific torque of at least 10 Nm/kg is required according to [1], [34]. Additional requirements for the electric motor in (quasi-)direct-drive actuators are given in Table I.

TABLE I
Application Requirements for Electric Motors in (Quasi-)Direct-Drive Robotic Actuators

| Requirement | Motivation |
|---|---|
| High (specific) torque | System specific torque $>$ 10Nm/kg [1], [34] |
| Low speed | Maximum 300 rpm in direct-drive applications [1], [2]<br>Maximum 3000 rpm for quasi-direct-drive applications [35] |
| Low DC bus voltage | To ensure sufficient electrical safety, a common DC bus voltage level is 48 V [36], [37]. |
| Pancake-shaped motor | Offers highest specific torque if the mass is constrained in low gear ratio actuators [3]. |

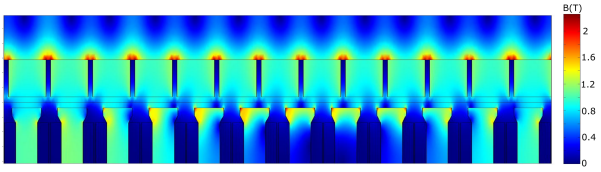


Fig. 2. 2D finite element magnetostatic simulation of the magnetic flux density at the inner radius for a phase current density of 5$A_{\mathrm{RMS}}$/mm$^2$

As already mentioned in the introduction, the YASA AFPMSM holds high potential to further push the specific torque limits for robotic applications [6]. Table II gives the design parameters of the test case YASA AFPMSM used in this work. The stator of the test case machine with anodised aluminium foil winding is shown in Fig. 1 for illustration. An analytical electromagnetic model for the flux distribution in the stator core from [38] was used to calculate the number of turns that satisfies the DC bus voltage and maximum speed requirements of Table I. The final design was simulated using a multislice 2D finite element magnetostatic model to check for excessive saturation in the stator teeth. Fig. 2 shows the magnetic flux density at the inner radius of the machine for a current density of 5 $A_{\mathrm{RMS}}/\mathrm{mm}^2$. It is clear that the stator teeth do not exhibit excessive saturation.

This test case machine is used throughout this work to evaluate the use of anodised aluminium foil. This is done by comparing its performance in terms of winding losses, thermal properties and specific torque to a benchmark situation. An electromagnetically identical machine with enamelled copper wire and with the same number of turns per tooth coil is chosen as benchmark because most electric motors in robotic applications use this type of conductor [36]. The conductor dimensions and properties for both the enamelled round copper wire and anodised aluminium foil are given in Table III. Note that the dielectric strength of the anodised aluminium foil conductors is more than three times lower compared to enamelled copper wire moreover, this dielectric strength strongly decreases with decreasing bending radius of the foil. Because aluminium-oxide is a ceramic material, it is brittle. Hairline cracks start to appear on the surface of the foil when it is bend. It was shown in [29] that when arcing happens,

TABLE II
SPECIFICATIONS OF THE TEST CASE YASA AFPMSM

| Parameter | Symbol | Value | Unit |
|---|---|---|---|
| Three-phase inverter DC bus voltage | $V_{\mathrm{DC}}$ | 48 | V |
| Maximum speed | $\Omega_{\mathrm{max}}$ | 300 | rpm |
| Number of pole pairs | $N_{\mathrm{p}}$ | 13 | / |
| Number of slots | $Q_{\mathrm{s}}$ | 24 | / |
| Number of phases | $n_{\mathrm{ph}}$ | 3 | / |
| Number of turns per tooth coil | $n_{\mathrm{turns}}$ | 35 | / |
| Outer diameter stator iron core | $D_{\mathrm{o}}$ | 138.5 | mm |
| Inner diameter stator iron core | $D_{\mathrm{i}}$ | 98.5 | mm |
| Axial length stator iron core | $h_{\mathrm{stat}}$ | 15 | mm |
| Axial slot length | $h_{\mathrm{slot}}$ | 10 | mm |
| Total axial length (incl. housing) | $l_{\mathrm{tot}}$ | 62.5 | mm |
| Slot width | $b_{\mathrm{slot}}$ | 6 | mm |
| Airgap thickness | $h_{\mathrm{air}}$ | 1.5 | mm |
| Magnet height | $h_{\mathrm{mag}}$ | 5 | mm |
| Rotor yoke height | $h_{\mathrm{mag}}$ | 6 | mm |

(a) (b)

Fig. 3. (a) CAD drawing of the test case YASA AFPMSM (b) Assembled prototype stator and rotor, both enamelled copper wire and anodised aluminium foil stator look identical after epoxy impregnation

it is typically between two opposed cracks. The manufacturer reported a breakdown voltage of 194.2 $V_{\mathrm{RMS}}$ for a bending radius of 5 mm, hence breakdown will not occur in the considered test case machine since the total DC bus voltage is only 48 V.

Fig.3a gives a CAD drawing of the test case machine, the realised prototype is shown in Fig. 3b. The stator is impregnated with epoxy resin for mechanical stability [6]. This also protects the edges of the foil which are very prone to deformation due to the limited thickness of the foil, the impregnation also improves the thermal conductivity [39]. The stator consists of 24 concentrated winding tooth coils as shown in Fig. 4. Its inherent segmented structure allows winding of the coils prior to assembly into the stator [6]. This simplifies the foil winding process and allows to avoid open slots or a segmented stator which are required in the case of a radial flux machine [32], [40]. It also allows to eliminate the free space in a slot as found between two adjacent winding phases in foil wound radial flux machines [32].

## III. WINDING LOSS EVALUATION AND COMPARISON

In this section, the influence of the use of anodised aluminium foil on the winding losses in comparison to copper wire will be discussed.

*1) DC winding resistance:* To compare the DC winding losses for both conductor materials, the DC resistance is


Fig. 4. Prototype tooth coils. Left: enamelled copper wire tooth coil, Right: anodised aluminium foil tooth coil

calculated using the law of Pouillet:

$$R_{\mathrm{DC}}(T) = \frac{\rho \cdot l \cdot (1 + \alpha \cdot (T - 20°\mathrm{C}))}{S} \tag{1}$$

Where $R_{\mathrm{DC}}$ is the DC winding resistance at temperature $T$, $\rho$ is the electrical resistivity at 20°C, $l$ is the total length of the winding and $S$ is the conductor cross-section. Using geometrical data obtained from the prototype tooth coils shown in Fig. 4, the DC resistance is calculated. For the copper wire tooth coil $R_{\mathrm{DC,Cu}}(T = 25°C) = 95.7\ m\Omega$ , and for the anodised aluminium foil tooth coil $R_{\mathrm{DC,Al}}(T = 25°C) = 101.9\ m\Omega$. This results in a theoretical ratio of copper wire coil DC resistance over anodised aluminium foil coil DC resistance of 0.94, whereas experimentally it was observed that this ratio is 0.99. This discrepancy can be explained by the fact that there can be some deviation in the electrical resistivity from its nominal value. The allowed deviation is specified in standard IEC 60317-0-1 for enamelled copper wire. For the anodised aluminium foil, no standards exists yet that specifies the allowed deviation on the electrical resistivity and the tolerances on the dimensions, therefore the deviation between the estimated and real value is larger than for the copper wire.

Note that although, the electric resistivity of aluminium is 59% larger compared to copper, the winding DC resistance of the anodised aluminium foil tooth coil is only 1% larger. This is mainly the consequence of the large difference in conductor cross-section. It is possible to use a larger cross-section for the foil coil because the foil winding configuration allows a more efficient utilization of the available slot space. This can also be seen when comparing the fill factors for both tooth coils in Table III, the fill factor is defined here as the number of turns times the conductor cross-section divided by the available slot space. In the test case machine the available slot space is 10 x 3.58 mm$^2$. Note that the anodised aluminium foil tooth coil weighs 18% less than its copper equivalent.

*2) AC winding resistance:* Several authors have studied AC winding losses in copper foil wound rotating electrical machines [23], [41]. They have concluded that AC winding losses can be an important part of the total winding losses especially in high-frequency machines. Therefore they recommended to use foil windings only in low frequency applications [41] and/or in case of short axial length in axial flux machines or short slot height in radial flux machines [42]. In direct-drive robotic applications where the maximum motor speed is typically low (300 rpm) and short axial length, pancake

TABLE III
SPECIFICATIONS OF THE PROTOTYPE TOOTH COIL

| **Enamelled copper wire (Grade I, IEC 60317-13)** | **Symbol** | **Value** | **Unit** |
|---|---|---|---|
| Number of turns | $n_{\text{turns}}$ | 35 | / |
| Nominal outer diameter | $d_{\text{Cu,o}}$ | 0.8425 | mm |
| Conductor diameter | $d_{\text{Cu,i}}$ | 0.8 | mm |
| Winding length (incl. terminals) | $l_{\text{Cu}}$ | 276 | cm |
| measured DC resistance (@ 25°C) | $R_{\text{DC,Cu}}$ | 94.54±0.37[1] | mΩ |
| Height laminated iron core | $h_{\text{core}}$ | 20 | mm |
| Weight of tooth coil | $m_{\text{Cu+SiFe}}$ | 31.3 | g |
| Resistivity copper | $\rho_{\text{Cu}}$ | $1.72 \cdot 10^{-8}$ | Ωm |
| Resistance temperature coeff. | $\alpha_{\text{Cu}}$ | $3.93 \times 10^{-3}$ | $K^{-1}$ |
| Fill factor | $f_{\text{Cu,coil}}$ | 49 | % |
| Dielectrical strength (IEC 60317-0-1) | $E_{\text{max}}$ | 87 | $V_{\text{RMS}}/\mu$m |
| Price/kg | | 16.64 | EUR/kg |
| **Anodised aluminium foil** | | | |
| Number of turns | $n_{\text{turns}}$ | 35 | / |
| foil width | $h_{\text{Al}}$ | 10 | mm |
| total foil thickness | $t_{\text{Al,tot}}$ | 86 | $\mu$m |
| thickness $Al_2O_3$ layer | $t_{\text{AlOx}}$ | 4.6 | $\mu$m |
| Foil length (excl. terminals) | $l_{\text{Cu}}$ | 250 | cm |
| Cu terminal length (dia. 0.9 mm) | $l_{\text{term}}$ | 40 | cm |
| measured DC resistance (@ 25°C) | $R_{\text{DC,Al}}$ | 95.83±0.6[1] | mΩ |
| Height laminated iron core | $h_{\text{core}}$ | 20 | mm |
| Weight of tooth coil | $m_{\text{Al+SiFe}}$ | 25.8 | g |
| Resistivity aluminium | $\rho_{\text{Al}}$ | $2.74 \cdot 10^{-8}$ | Ωm |
| Resistance temperature coeff. | $\alpha_{\text{Al}}$ | $4.03 \times 10^{-3}$ | $K^{-1}$ |
| Fill factor | $f_{\text{Al,coil}}$ | 75 | % |
| Dielectrical strength (ISO 2376) | $E_{\text{max}}$ | 26.5 | $V_{\text{RMS}}/\mu$m |
| Price/kg | | 685[2] | EUR/kg |

[1]mean and standard deviation over 24 tooth coils
[2]Note that this is the cost for a small order quantity of 2 kg, for larger order quantities the cost will be lower.

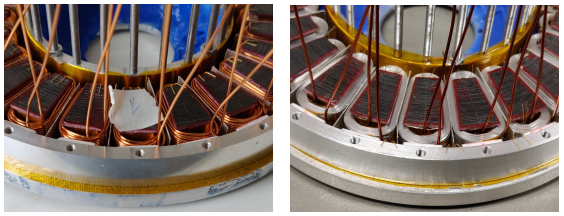

(a) (b)

Fig. 5. Enamelled copper wire (a) and anodised aluminium foil (b) stator prototypes prior to epoxy impregnation

shaped motors are frequently used, these recommendation are typically fulfilled. A prototype YASA AFPMSM with both anodised aluminium foil and enamelled copper wire as specified in Table II and III respectively is constructed as shown in Figures 3 and 5. The phase winding resistance of both prototypes was measured for various frequencies using an LCR-meter (Rhode and Schwarz HM 8118). Fig. 6 provides the ratio of phase resistance $R_{\text{DC+AC}}$ over DC phase resistance as a function of the electrical excitation frequency at 25°C. The circles indicate measured data points. For the maximum excitation frequency of the prototype YASA AFPMSM (65 Hz @ 300 rpm), the resistance increase for both the anodised aluminium foil and copper wire variant, remains below 0.5%. However, at higher frequencies, Fig. 6 confirms the findings of the authors in [23], [41] that foil windings suffer from higher AC losses. This is also illustrated clearly in Fig. 7,

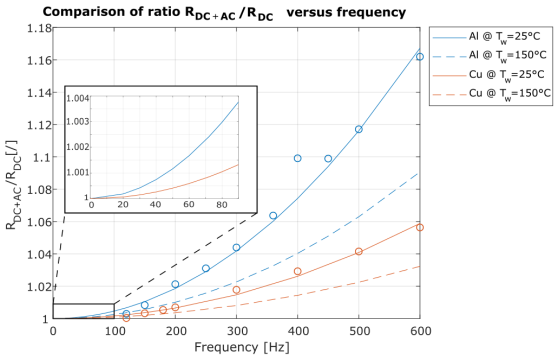


Fig. 6. Comparison of the $R_{\text{DC+AC}}/R_{\text{DC}}$ ratio between the anodised aluminium foil and copper wire prototype YASA AFPMSM as a function of the electrical excitation frequency, both for 25°C (measured data points are indicated with circles) and 150°C (trendline calculated according to [43])

where the ratio $R_{\text{AC}}/R_{\text{DC}}$ is plotted. This allows to determine the frequency where $R_{\text{AC}}$ becomes larger than to $R_{\text{DC}}$. This is called the crossover frequency $f_{\text{crossover}}$. For the anodised aluminium foil winding, this is already at 1466 Hz, whereas for the enamelled copper wire winding this is only at 2492 Hz.

In contrast to the DC resistance, the AC resistance decreases for increasing temperatures. Equation 2 from [43] was used to calculate the ratio $R_{\text{DC+AC}}/R_{\text{DC}}$ for an average winding temperature of $T = 150$°C using experimental data obtained at $T_0 = 25$°C:

$$(R_{\text{DC+AC}}/R_{\text{DC}})|_{\text{T}} = \frac{(R_{\text{DC+AC}}/R_{\text{DC}})|_{\text{T}_0} - 1}{(1 + \alpha(T - T_0))^{\frac{3}{2}}} + 1 \qquad (2)$$

With $\alpha$ the temperature coefficient of resistivity for copper and aluminium respectively from Table III. The resulting graphs are plotted in dashed lines in Fig. 6. The anodised aluminium foil coil still exhibits a higher AC resistance. However, the difference in AC resistance between the anodised aluminium foil coil and copper wire coil decreases at higher temperatures. Since the AC resistance at the maximum excitation frequency of the prototype motor at ambient temperature could be neglected, and it decreases with increasing temperature, the AC losses are neglected in the remainder of this work.

## IV. THERMAL PERFORMANCE EVALUATION AND COMPARISON

This section aims to study the influence of the use of anodised aluminium foil on the stator thermal performance in comparison to enamelled copper wire. The thermal performance of anodised aluminium foil and enamelled copper wire will be compared through both thermal measurements on a tooth coil, stator and a rotating motor, and through 3D thermal FE simulations. The parameters of the 3D thermal FE model will be determined experimentally through a similar procedure as described in [44]. The 3D thermal FE model is then used to study the influence of the winding-housing thermal interface and cooling on the thermal performance for both conductor materials

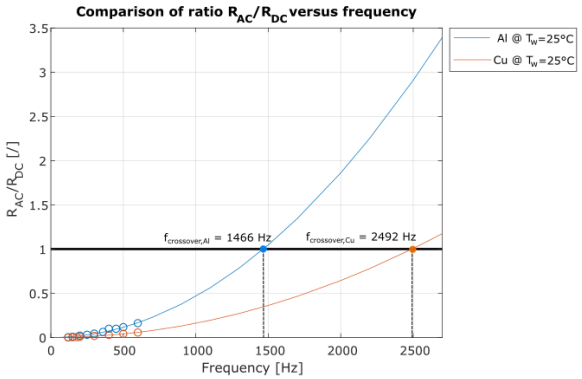


Fig. 7. Comparison of the $R_{\mathrm{AC}}/R_{\mathrm{DC}}$ ratio between the anodised aluminium foil and copper wire prototype YASA AFPMSM as a function of the electrical excitation frequency (measured data points are indicated with circles), the frequency where $R_{\mathrm{AC}}$ becomes larger than $R_{\mathrm{DC}}$ is denoted by $f_{\mathrm{crossover}}$

### *A. Identification and comparison of equivalent thermal conductivities*

A winding body is an amalgam of different materials: conductor, insulation and impregnation material. However, it is difficult to represent all these materials individually in a thermal FE model [39]. Several authors have overcome this issue through homogenization of the winding body in which a winding body is considered as a homogeneous material with an equivalent thermal conductivity tensor depending on the conductivities of the constituting materials [6], [39]. In this paragraph, the unknown equivalent thermal conductivity parameters for a 3D thermal FE model are determined by fitting the thermal FE model steady-state temperature predictions to temperatures measured on a dedicated identification tooth coil setup.

The anodised aluminium foil winding body consists of stacked layers of aluminium, aluminium oxide and epoxy impregnation. Since the thermal conductivity of aluminium is much larger, the equivalent thermal conductivity in the plane of the foil will be much larger than perpendicular to this plane. To include this phenomenon, one equivalent thermal conductivity for the good thermally conducting direction (in the plane of the foil) and one for the poor thermally conducting direction (perpendicular to the foil) are defined. Instead of directly fitting the equivalent thermal conductivities, they are first expressed in terms of the volume fractions (or fill factor) and thermal conductivities of the constituting materials. A grid search over these parameters is then performed to identify the parameters that result in the best fit between measurements and FE model predictions. For the good thermally conducting direction, the equivalent thermal conductivity can be calculated using the parallel material model from [39]:

$$k_{1,\mathrm{wi}}^{\mathrm{Al}} = f_{\mathrm{wi}}^{\mathrm{Al}} \cdot k_{1,\mathrm{anofol}} + (1 - f_{\mathrm{wi}}^{\mathrm{Al}}) \cdot k_{\mathrm{Ep}} \tag{3}$$

Where $f_{\mathrm{wi}}^{\mathrm{Al}}$ is the fill factor of the impregnated winding body, $k_{1,\mathrm{anofol}}$, the equivalent thermal conductivity of the anodised foil in the plane of the foil and $k_{\mathrm{Ep}}$, the thermal conductivity of the epoxy resin. For the thermally poor conducting direction, the equivalent thermal conductivity can be calculated using the series material model from [39]:

$$k_{2,\mathrm{wi}}^{\mathrm{Al}} = \frac{k_{2,\mathrm{anofol}} \cdot k_{\mathrm{Ep}}}{(1 - f_{\mathrm{wi}}^{\mathrm{Al}}) \cdot k_{2,\mathrm{anofol}} + f_{\mathrm{wi}}^{\mathrm{Al}} \cdot k_{\mathrm{Ep}}} \tag{4}$$

Where $k_{2,\mathrm{anofol}}$ is the equivalent thermal conductivity of the anodised foil perpendicular to the plane of the foil. $k_{1,\mathrm{anofol}}$ and $k_{2,\mathrm{anofol}}$ are also determined using the parallel and series material models respectively for the aluminium - aluminium-oxide amalgam:

$$k_{1,\mathrm{anofol}} = f_{\mathrm{anofol}} \cdot k_{\mathrm{Al}} + (1 - f_{\mathrm{anofol}}) \cdot k_{\mathrm{AlOx}} \tag{5}$$

$$k_{2,\mathrm{anofol}} = \frac{k_{\mathrm{Al}} \cdot k_{\mathrm{AlOx}}}{(1 - f_{\mathrm{anofol}}) \cdot k_{\mathrm{Al}} + f_{\mathrm{anofol}} \cdot k_{\mathrm{AlOx}}} \tag{6}$$

With $k_{\mathrm{Al}}$ and $k_{\mathrm{AlOx}}$, the thermal conductivity of aluminium and aluminium-oxide respectively. The fill factor for this combination is defined as:

$$f_{\mathrm{anofol}} = \frac{t_{\mathrm{Al,tot}} - 2 \cdot t_{\mathrm{AlOx}}}{t_{\mathrm{Al,tot}}} \tag{7}$$

For the epoxy impregnated, enamelled copper wire winding body, the equivalent thermal conductivities are calculated through the use of the Hashin and Shriktman approximation [39]:

$$k_{1,\mathrm{wi}}^{\mathrm{Cu}} = f_{\mathrm{wi}}^{\mathrm{Cu}} \cdot k_{\mathrm{Cu}} + (1 - f_{\mathrm{wi}}^{\mathrm{Cu}}) \cdot k_{\mathrm{Ep}} \tag{8}$$

$$k_{2,\mathrm{wi}}^{\mathrm{Cu}} = k_{\mathrm{Ep}} \cdot \frac{(1 + f_{\mathrm{wi}}^{\mathrm{Cu}}) \cdot k_{\mathrm{Cu}} + (1 - f_{\mathrm{wi}}^{\mathrm{Cu}}) \cdot k_{\mathrm{Ep}}}{(1 - f_{\mathrm{wi}}^{\mathrm{Cu}}) \cdot k_{\mathrm{Cu}} + (1 + f_{\mathrm{wi}}^{\mathrm{Cu}}) \cdot k_{\mathrm{Ep}}} \tag{9}$$

With $f_{\mathrm{wi}}^{\mathrm{Cu}}$ the fill factor the the impregnated copper coil and $k_{\mathrm{Cu}}$, the thermal conductivity of copper.

The fill factors $f_{\mathrm{wi}}^{\mathrm{Cu}}$ and $f_{\mathrm{wi}}^{\mathrm{Al}}$ and $k_{\mathrm{Ep}}$ will now be determined through experimental parameter identification. To this end, a dedicated identification tooth coil was constructed and equipped with temperature sensors at critical locations. These locations were determined based on insights from [6]. Fig. 8 shows the stator teeth that are used for identification, the locations of the temperature sensors in the centre half plane are indicated with red dots. An equal and constant power is dissipated in both coils and the steady-state temperatures are recorded. To keep the power constant, the current has to be adjusted to compensate for the increase in DC resistance at higher temperatures. To obtain similar conditions as in the prototype YASA AFPMSM (Fig. 3) where the heat dissipation via the air gap is assumed to be negligible [6], all faces of the sample are insulated with thermal insulating wool except the aluminium housing '1', which is cooled by natural convection. Two aluminium-oxide pads are inserted between the housing and the conductor material to guarantee sufficient electrical insulation without adding significant thermal resistance. Fig. 9 shows the modelled geometry of the corresponding FE model. Due to thermal symmetry, it is sufficient to model only one quarter of a single tooth coil. It consists of 5 different domains with different thermal properties. It is assumed that all heat is evacuated from the motor via the outer radial surface of the aluminium housing via convection. In agreement with the tooth coil samples, thermal insulation is assumed for all other faces. The fill factor $f_{\mathrm{wi}}^{\mathrm{x}}$ (x = {Al,Cu}) and epoxy thermal conductivity $k_{\mathrm{Ep}}$ are identified through a grid search

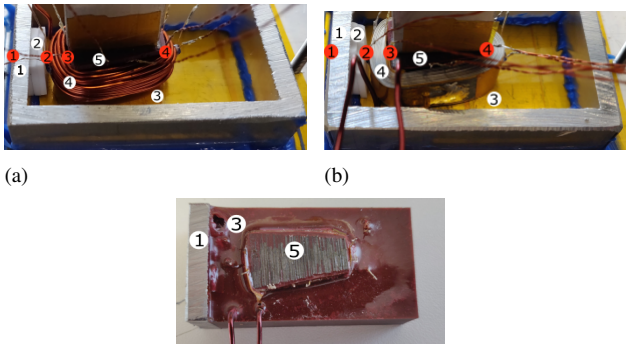

(a) (b) (c)

Fig. 8. Mock-up stator tooth for identification of fill factor and thermal conductivity of epoxy (a & b prior to impregnation, c after impregnation): (1) Aluminium housing (2) Aluminium-oxide pads (3) Epoxy impregnation (4a) Enamelled copper wire (4b) Anodised aluminium foil (5) Iron core; Red dots indicate PT100 temperature sensor locations

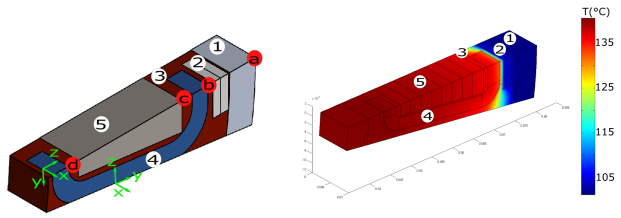


(a) (b)

Fig. 9. (a) 3D Thermal FEM quarter tooth coil model (b) Temperature distribution for 3.6 W losses in the aluminium winding: (1) Aluminium housing (2) Aluminium oxide thermal pad (3) Epoxy (4) Anodised aluminium foil or enamelled copper wire (5) Iron core; The red dots indicate the temperature sensor locations

over all possible combinations to find the combination which minimizes the cost:

$$\min_{\forall f_{\mathrm{wi}}^{\mathrm{x}},k_{\mathrm{Ep}}} \sum_{i=2}^{4} (T_{\mathrm{i}}^{\mathrm{FE}}(f_{\mathrm{wi}},k_{\mathrm{Ep}}) - T_{\mathrm{i}}^{\mathrm{meas}})^2 \text{ for x=\{Al,Cu\}} \quad (10)$$

$T_{\mathrm{i}}^{\mathrm{FE}}$ and $T_{\mathrm{i}}^{\mathrm{meas}}$ are the predicted and measured temperatures at location $i$ respectively. The locations are indicated on Fig. 8 . The results of the identification are given in Table IV. The equivalent thermal conductivities $k_{\mathrm{x}}$, $k_{\mathrm{y}}$, $k_{\mathrm{z}}$ are calculated using equations 3 through 9.

The equivalent thermal conductivity for the thermally poor conducting direction, $k_{\mathrm{z}}$, of the anodised aluminium foil is 3.6 times larger than for the copper coil. Moreover $k_{\mathrm{z}}$ of the anodised aluminium foil winding is in good agreement with the values reported for an anodised aluminium wire amalgam in [16], [24], [39], confirming the validity of the modelling and estimation procedure. Note that a temperature sensor at location '1' is an absolute requirement for the unique identification of the parameters, however this is only possible in a mock-up setup because the temperature sensor creates an epoxy-filled gap between the winding and the aluminium-oxide pads which significantly increases the thermal resistance as will be shown in the following paragraph.

TABLE IV
EXPERIMENTALLY IDENTIFIED THERMAL PARAMETERS

| Parameter | Anodised aluminium | | Enamelled copper | |
|---|---|---|---|---|
| $f_{\mathrm{wi}}^{\mathrm{x}}$ [/] | 0.9 | | 0.33 | |
| $k_{\mathrm{Ep}}$ [W/mK] | 0.73 | | 0.73 | |
| $k_{\mathrm{x}}$ [W/mK] | $k_{1,\mathrm{wi}}^{\mathrm{Al}}$ | 212 | $k_{2,\mathrm{wi}}^{\mathrm{Cu}}$ | 1.37 |
| $k_{\mathrm{y}}$ [W/mK] | $k_{1,\mathrm{wi}}^{\mathrm{Al}}$ | 212 | $k_{1,\mathrm{wi}}^{\mathrm{Cu}}$ | 124 |
| $k_{\mathrm{z}}$ [W/mK] | $k_{2,\mathrm{wi}}^{\mathrm{Al}}$ | 7.1 | $k_{2,\mathrm{wi}}^{\mathrm{Cu}}$ | 1.37 |

### *B. Stator thermal performance and influence of winding-housing thermal interface*

The influence of the conductor material on the stator performance is analysed in this section using the identified parameters from Section IV-A in a 3D thermal FE model. The FE model from Section IV-A is adapted by removing the gap between the winding body and the aluminium-oxide pads created by the temperature sensor. However, a small void or gap remains because of the irregularity of the winding body top surface. Due to the low viscosity of the used epoxy, this gap is also filled with epoxy during impregnation. Despite the irregular and complex geometry of this gap, it is represented by an equivalent thin layer with uniform thickness $t_{\mathrm{gap,equi}}$ in the 3D thermal FE model. However, this equivalent gap thickness is difficult to determine a priori and strongly depends on the material and manufacturing tolerances. Therefore influence of the conductor material on the stator thermal performance is analysed as a function of the equivalent fill factor of the space between the winding body and the housing $f_{\mathrm{interface}}$, which is defined by:

$$f_{\mathrm{interface}} = \frac{t_{\mathrm{AlOx\text{-}pads}}}{t_{\mathrm{AlOx\text{-}pads}} + t_{\mathrm{gap,equi}}} \quad (11)$$

With $t_{\mathrm{AlOx\text{-}pads}}$, the thickness of the aluminium-oxide thermal pads between the winding body and housing. The stator thermal performance will be expressed in terms of the thermal resistance between the hotspot and the outer surface of the housing:

$$R_{\mathrm{hotspot}} = \frac{T_{\mathrm{hotspot}} - T_{\mathrm{housing}}}{P_{\mathrm{dissipated\ losses}}} \quad (12)$$

The hotspot location coincides with the location of temperature sensor 'd' [6]. The hotspot temperature is of interest because the losses (and thus the torque) for which this temperature corresponds to the material temperature limit, determines the specific torque. The thermal FE model with parameters from Table IV is used to calculate $R_{\mathrm{hotspot}}$ for both the anodised aluminium foil and copper wire winding stators as a function of $f_{\mathrm{interface}}$. The results are given in Fig. 10. Over the complete range of $f_{\mathrm{interface}}$ the thermal resistance of the anodised aluminium foil winding stator is lower compared to the copper wire winding stator, this could be expected from the results in Section IV-A, however it should be noted that the relative difference in thermal resistance increases for increasing $f_{\mathrm{interface}}$. The temperature difference $[T_{\mathrm{Cu\text{-}wire}} - T_{\mathrm{Al\text{-}foil}}]_{\forall(\mathrm{x,y,z})}$ is plotted for two extreme cases $f_{\mathrm{interface}} = 1$ and $f_{\mathrm{interface}} = 0.5$. For the ideal case of $f_{\mathrm{interface}} = 1$, the thermal resistance of the aluminium stator is 39% lower compared to its copper counterpart, whereas for $f_{\mathrm{interface}} = 0.5$, representing a very

poor thermally conducting interface between winding body and housing, it is only 4% lower.

The true thermal resistance between the hotspot and the housing was measured for both conductor materials, both in a single stator tooth and a full stator prototype as shown in Fig. 11. Fig. 11a and b show the tooth coils prior to epoxy impregnation. After epoxy impregnation the samples look identical to Fig. 8c. The small gap between winding body and thermal pads is indicated with a red circle. During the measurements all surfaces are thermally insulated with thermal insulating wool except the aluminium housing surface '1' which is cooled by natural convection. Fig. 11c shows the stator prototype after epoxy impregnation. Both copper and aluminium winding prototypes look identical after impregnation. The top and bottom surface are insulated with XPS insulation, however for clarity the top insulating cover is not shown on Fig. 11c. The stator prototypes are cooled via a water cooled cold plate. The motor aluminium housing '1' is thermally connected via silicone thermal pads '9', an aluminium interconnection shell '10', and silicone thermal paste '11' to the aluminium cold plate '8'. The thermal resistance was determined by dissipating a constant and equal power in both winding bodies and recording the steady-state hotspot 'd' and housing temperature 'a'. For the full stator prototype, the average over 8 different coils is used. To keep the power constant, the current has to be adjusted to compensate for the increase in DC resistance at higher temperatures. The results are indicated on Fig. 10. This allows to estimate the $f_{\text{interface}}$ for the tooth coil and stator prototypes from Fig. 11. In all cases, the estimated fill factor $f_{\text{interface}} < 1$, thus confirming the presence of epoxy between the winding body and the aluminium-oxide thermal pads. The reduction in thermal resistance compared to a winding body with enamelled copper wire is 14% for the tooth coil prototypes and 1% in favour of copper for the full stator prototypes. The latter is caused by a lower $f_{\text{interface}}$ for the aluminium winding stator case due to tolerances in the manufacturing process of the prototype. These results allows us to conclude that the use of anodised aluminium foil can only result in a significantly lower thermal resistance between hotspot and housing in case the winding body represents a significant fraction of this thermal resistance.

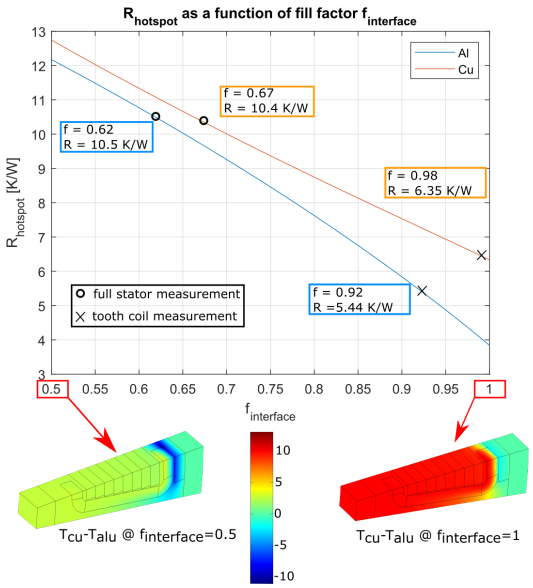


Fig. 10. (Top) Thermal resistance between hotspot and housing as a function of the fill factor $f_{\text{interface}}$ of the thermal interface between winding and housing for both anodised aluminium foil and copper wire winding stators, 'circles' indicate measurements on a full stator and 'x' indicates measurements on a tooth coil
(bottom) $[T_{\text{Cu-wire}} - T_{\text{Al-foil}}]_{\forall(x,y,z)}$ for $f_{\text{interface}} = 0.5$ (left) and $f_{\text{interface}} = 1$ (right)

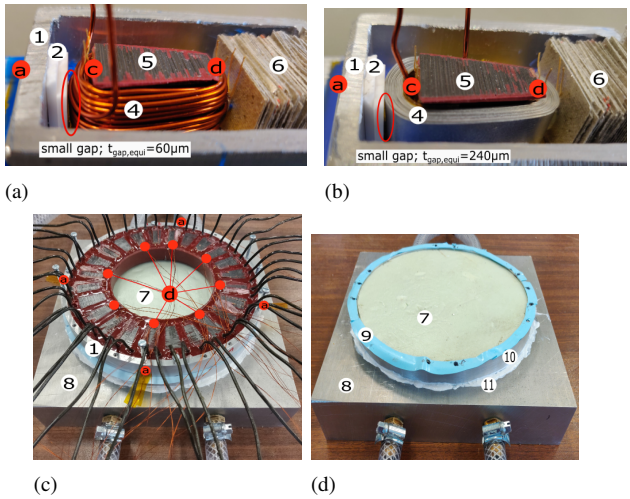


Fig. 11. (a and b) stator tooth coil prototype prior to epoxy impregnation (c) full stator prototype on cold plate: aluminium and copper variant look identical after impregnation (d) thermal interface between stator prototype and cold plate. (1) Aluminium housing (2) Aluminium-oxide pads (4a) Enamelled copper wire (4b) Anodised aluminium foil (5) Iron core (6) Mica paper stack, to press winding body against thermal pads (7) XPS insulation (8) Cold plate (9) Silicone thermal pad (10) Aluminium interconnection shell (11) Silicone thermal paste. Red dots indicate PT100 temperature sensor locations

## V. SPECIFIC TORQUE COMPARISON

In previous sections, the losses and thermal properties have been studied since both aspects affect the specific torque of an electrical machine. In this section, the specific torque of the anodised aluminium foil and copper wire test case YASA AFPMSM are determined experimentally on a rotating setup. Additionally, experimental loss data and the 3D thermal FE model from section IV are used to study the influence of the cooling performance on the specific torque.

### *A. prototype YASA AFPMSM scenario*

The prototype YASA AFPMSMs are compared experimentally on a rotating test bench both under same hotspot temperature conditions (i.e. the hotspot in both motors is identical) and under same current conditions (i.e. the phase current in both motors is identical) One set of bearings and rotor discs was used for both motors to eliminate as many error sources as possible. Fig. 12 shows the testbench that was used to determine the specific torque. The prototype YASA AFPMSM as shown in Fig. 3 is connected via a torque sensor (Lorenz DR-2112, ±50 Nm) to a load motor. A magnetic absolute encoder (RLS AksIM-2) was used to measure the

position. The YASA AFPMSM is supplied from a custom three-phase two-level voltage source inverter ($V_{\text{DC}} = 48V$) and uses Allegro ACS730KLCTR-40AB-T phase current sensors, a dSPACE MicroLabBox was used to implement standard field oriented PI current controllers. The same temperature sensors as indicated on Fig. 11c are used to measure the hotspot temperature. The YASA AFPMSM housing is thermally insulated from its mounting flange via 0.4 mm mica sheet and cooled via natural convection over its radial and axial housing surface. The results are given in Table V and VI. In the

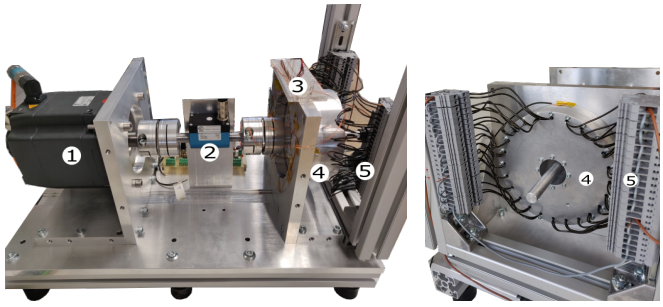


(a) (b)

Fig. 12. Prototype testbench: (1) Load motor (2) Torque sensor (Lorenz DR-2112, ±50 Nm) (3) PT100 terminal board (4) prototype YASA AFPMSM, both aluminium and copper variant look identical (5) motor terminal interconnection rail

'same hotspot temperature'-scenario, the anodised aluminium foil wound prototype shows a 13% increase with respect to the copper winding variant in terms of torque per kg active stator mass. However, in terms of the other metrics, the copper winding variant shows a better performance. This is explained by the fact that the copper wire winding prototype exhibits a higher torque constant and a slightly lower thermal resistance (see Fig. 10). The difference in thermal resistance was already explained in Section IV-B. The difference in torque constant is the consequence of small differences between the two prototypes in the radial positions of the stator teeth. This was caused by the manual manufacturing process. In the 'same phase current'-scenario , it can be seen in Table VI that the winding losses in the aluminium foil motor are slightly higher, due to its slightly larger DC resistance. Also the hotspot temperature is larger due to the larger losses and the larger thermal resistance. Despite its lower torque constant and slightly higher thermal resistance, the anodised aluminium foil winding prototype YASA AFPMSM still demonstrates a higher torque per kg of active stator mass on the testbench. This affirms the potential of anodised aluminium foil wound YASA AFPMSMs to obtain a higher specific torque compared to enamelled copper wire variants.

The measured efficiency of both motors is also given in Table V and VI. The efficiency is quite low because of the low operating speed. Note however that it was not the aim of this study to optimize efficiency.

In Fig. 13, the measured transient thermal response of the housing and hotspot temperatures for a step change in the winding losses are given for both the anodised aluminium foil and copper wire winding prototype motors operating at 300 rpm. It should be noted that no significant difference

TABLE V
COMPARISON OF PROTOTYPE YASA AFPMSM @ [$\Omega_m$ =300 RPM, $T_{\text{HOTSPOT}} = 61.35°C$, $T_{\text{AMBIENT}} = 25°C$]

| | **Anodised Aluminium foil** | **Enamelled Cu wire** | **Al/Cu** |
|---|---|---|---|
| Phase current [$A_{\text{RMS}}$] | 3.47 | 3.62 | 0.96 |
| $T_{\text{hotspot}}$ [$°C$] | 61.4 | 61.4 | 1 |
| Torque [Nm] | 2.88 | 3.09 | 0.93 |
| Torque constant [Nm/A] | 0.83 | 0.85 | 0.97 |
| Efficiency (%) | 69 | 71 | 0.97 |
| **Specific Torque** | | | |
| Nm/kg active stator mass | 4.65 | 4.11 | 1.13 |
| Nm/kg active mass | 1.24 | 1.25 | 0.99 |
| Nm/kg active+non-active mass | 0.83 | 0.86 | 0.97 |
| **Torque density** | | | |
| Nm/litre active stator volume | 10.6 | 11.35 | 0.93 |
| Nm/litre active volume | 4.77 | 5.12 | 0.93 |
| **Power and Losses** | | | |
| $P_{\text{DC}}$, DC input power [W] | 128 | 136 | 0.94 |
| $P_m$, mechanical power [W] | 90.6 | 97.0 | 0.93 |
| $P_{\text{no-load}}$ no-load losses [W][1] | 4.60 | 4.56 | 1.01 |
| $P_{\text{PE}}$, inverter losses[W][2] | 1.86 | 2.01 | 0.93 |
| $P_{\text{w}}$, winding losses [W][3] | 30.6 | 32.5 | 0.94 |

TABLE VI
COMPARISON OF PROTOTYPE YASA AFPMSM @ [$\Omega_m$ =300 RPM, PHASE CURRENT = 3.62 $A_{\text{RMS}}$, $T_{\text{AMBIENT}} = 25°C$]

| | **Anodised Aluminium foil** | **Enamelled Cu wire** | **Al/Cu** |
|---|---|---|---|
| Phase current [$A_{\text{RMS}}$] | 3.62 | 3.62 | 1 |
| $T_{\text{hotspot}}$ [$°C$] | 63.5 | 61.4 | 1.03 |
| Torque [Nm] | 2.92 | 3.09 | 0.93 |
| Torque constant [Nm/A] | 0.81 | 0.85 | 0.95 |
| Efficiency (%) | 69 | 71 | 0.97 |
| **Specific Torque** | | | |
| Nm/kg active stator mass | 4.71 | 4.11 | 1.15 |
| Nm/kg active mass | 1.26 | 1.25 | 1.01 |
| Nm/kg active+non-active mass | 0.84 | 0.86 | 0.98 |
| **Torque density** | | | |
| Nm/litre active stator volume | 10.74 | 11.35 | 0.95 |
| Nm/litre active volume | 4.84 | 5.12 | 0.94 |
| **Power and Losses** | | | |
| $P_{\text{DC}}$, DC input power [W] | 132.5 | 136 | 0.97 |
| $P_m$, mechanical power [W] | 92 | 97.0 | 0.95 |
| $P_{\text{no-load}}$ no-load losses [W][1] | 4.9 | 4.56 | 1.07 |
| $P_{\text{PE}}$, inverter losses[W][2] | 2.01 | 2.01 | 1 |
| $P_{\text{w}}$, winding losses [W][3] | 33.59 | 32.5 | 1.03 |

[1]Measured mechanical power when $I_{\text{phase}} = 0$; includes mechanical losses and iron losses
[2]Determined via transient calorimetric loss measurement method from [45]
[3]$P_w = P_{\text{DC}} - P_m - P_{\text{no-load}} - P_{\text{PE}}$

in transient behaviour could be observed on this time scale because the thermal time constant is mainly determined by the housing and mounting frame. Additionally, the estimated transient thermal responses are shown in Fig. 13. The 3D thermal FE model from Section IV-B was adapted and used to calculate the responses. A convective boundary condition was used for the airgap surface and the mounting frame was included into the model. The unknown parameters were identified through a grid search to find the parameters for which the estimated temperature rise best fitted the measured temperature rise. The good agreement between estimated and measured temperature rise again confirms the validity of the modelling approach followed in Section IV.

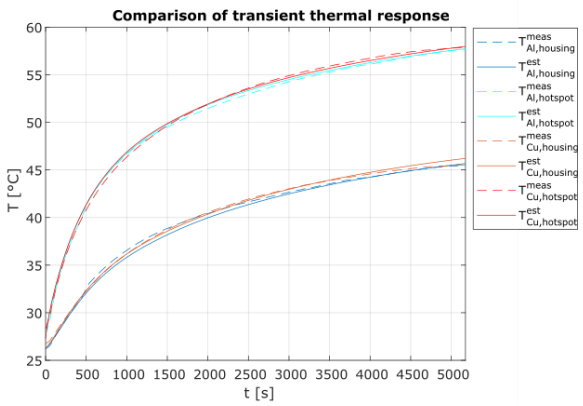


Fig. 13. Comparison of the predicted and measured temperature rise of the housing and the hotspot (location 'd' in Fig. 11) for a step change in the winding losses from 0 W to 30.5 W. The winding losses are kept constant during the transient by adjusting the $q$-axis current. The operating speed is kept constant to $\Omega_m$ = 300 rpm

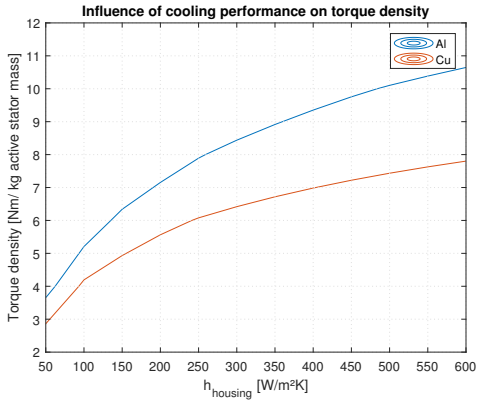


Fig. 14. Torque per kg of active stator mass comparison as a function of the convective heat transfer coefficient of the motor housing surface $h_{\text{housing}}$ @ [$\Omega_m$ = 300 rpm, $T_{\text{hotspot}} = 150°C$, $T_{\text{ambient}} = 50°C$]

### *B. Improved winding body thermal interface scenario and influence of cooling performance*

In this section, the specific torque is determined for the ideal case $f_{\text{interface}} = 1$ described in Section IV-B in function of the cooling performance. To this end, the thermal FE model from Section IV-B is used with the losses determined in Section III. A convective boundary condition on the motor housing is assumed with convective heat transfer coefficient $h_{\text{housing}}$ which is varied in order to examine the influence of the cooling performance. The results are given in Fig. 14. The anodised aluminium foil winding prototype has a higher specific torque per kg of active stator mass over the complete range of $h_{\text{housing}}$. The difference between the aluminium and copper winding variants increases for increasing cooling performance. This is in agreement with the findings from Section IV-B. The more dominant the winding body becomes in the thermal resistance between the hotspot and the ambient, the larger the difference in favour of the aluminium winding body caused by its higher equivalent thermal conductivities. In case of a high performance cooling system ($h_{\text{housing}} = 600\text{W/m}^2\text{K}$), the anodised aluminium foil winding test case machine exhibits a 37% higher torque per kg active stator volume.

## VI. Conclusion

In this work, the use of anodised aluminium foil as an alternative to enamelled copper wire was considered to improve the specific torque of a YASA AFPMSM for a direct-drive robotic application. Anodised aluminium foil allows a higher fill factor. This resulted in an almost equal DC resistance for a test case YASA AFPMSM. The higher thermal conductivity of the aluminium-oxide insulation and the foil topology result in higher equivalent thermal conductivities of the winding body. Both the higher fill factor and the better thermal properties contribute to a higher specific torque. A 13% increase in specific torque per kg active stator volume was measured experimentally for a test case YASA AFPMSM. Relying on experimental data and a 3D thermal FE model, it was shown that anodised aluminium foil winding offers a higher specific torque in low speed YASA axial flux motors where the winding body thermal resistance is dominant in the thermal path from heat source to heat sink.

To conclude, the potential of anodised aluminium foil YASA AFPMSM to push the specific torque limit of direct-drive robotic actuators was clearly illustrated in this work. Despite the improvement, the resulting specific torque of the prototype motor is still far below the required 10 Nm/kg to realise useful tasks [1], [34]. Advanced cooling strategies and integration of electronics and motor can be considered to further push the specific torque limit.

## References

[1] J. Hollerbach, I. Hunter, J. Lang, S. Umans, R. Sepe, E. Vaaler, and I. Garabieta, "The mcgill/mit direct drive motor project," pp. 611–617. IEEE Comput. Soc. Press.

[2] G. Kenneally, A. De, and D. E. Koditschek, "Design principles for a family of direct-drive legged robots," *IEEE Robotics and Automation Letters*, vol. 1, pp. 900–907, 7 2016.

[3] P. M. Wensing, A. Wang, S. Seok, D. Otten, J. Lang, and S. Kim, "Proprioceptive actuator design in the mit cheetah: Impact mitigation and high-bandwidth physical interaction for dynamic legged robots," *IEEE Transactions on Robotics*, vol. 33, pp. 509–522, 6 2017.

[4] S. Yu, T. H. Huang, X. Yang, C. Jiao, J. Yang, Y. Chen, J. Yi, and H. Su, "Quasi-direct drive actuation for a lightweight hip exoskeleton with high backdrivability and high bandwidth," *IEEE/ASME Transactions on Mechatronics*, vol. 25, pp. 1794–1802, 8 2020.

[5] B. Zhang, T. Seidler, R. Dierken, and M. Doppelbauer, "Development of a yokeless and segmented armature axial flux machine," *IEEE Transactions on Industrial Electronics*, pp. 1–1, 2015.

[6] H. Vansompel, P. Leijnen, and P. Sergeant, "Multiphysics analysis of a stator construction method in yokeless and segmented armature axial flux pm machines," *IEEE Transactions on Energy Conversion*, vol. 34, pp. 139–146, 2019.

[7] J. Klassen, S. Chamberlain, and H. K. Ka, "Electric machine comprising a safety ring," Patent, 2018.

[8] M. Waldhof, A. Echle, and N. Parspour, "A novel drive train concept for personalized upper body exoskeletons with a multiphase axial flux machine," pp. 2160–2166. IEEE, 5 2019.

[9] C. Wohlers, P. Juris, S. Kabelac, and B. Ponick, "Design and direct liquid cooling of tooth-coil windings," *Electrical Engineering*, vol. 100, pp. 2299–2308, 12 2018.

[10] J. D. Widmer, C. M. Spargo, G. J. Atkinson, and B. C. Mecrow, "Solar plane propulsion motors with precompressed aluminum stator windings," *IEEE Transactions on Energy Conversion*, vol. 29, pp. 681–688, 9 2014.

[11] C. R. Sullivan, "Aluminum windings and other strategies for high-frequency magnetics design in an era of high copper and energy costs," pp. 78–84. IEEE, 2 2007.

[12] G. Cakal and O. Keysan, "Flat winding made of aluminum or copper sheet for axial flux machines," *IET Electric Power Applications*, vol. 15, pp. 429–440, 4 2021.
[13] A. Acquaviva, M. Diana, B. Raghuraman, L. Petersson, and S. Nategh, "Sustainability aspects of electrical machines for e-mobility applications part ii: Aluminium hairpin vs. copper hairpin," pp. 1–6. IEEE, 10 2021.
[14] A. Selema, M. N. Ibrahim, and P. Sergeant, "Additively-manufactured ultra-light shaped-profile windings for hf electrical machines and weight-sensitive applications," *IEEE Transactions on Transportation Electrification*, pp. 1–1, 2022.
[15] P. Arumugam, E. Amankwah, A. Walker, and C. Gerada, "Design optimization of a short-term duty electrical machine for extreme environment," *IEEE Transactions on Industrial Electronics*, vol. 64, pp. 9784–9794, 12 2017.
[16] R. Wrobel, N. Simpson, P. H. Mellor, J. Goss, and D. A. Staton, "Design of a brushless pm starter generator for low-cost manufacture and a high-aspect-ratio mechanical space envelope," *IEEE Transactions on Industry Applications*, vol. 53, pp. 1038–1048, 3 2017.
[17] M. Groninger, F. Horch, A. Kock, M. Jakob, and B. Ponick, "Cast coils for electrical machines and their application in automotive and industrial drive systems," pp. 1–7. IEEE, 9 2014.
[18] M. Bach, A. Babl, and D. Gerling, "Integration of forming manufacturing technology into the component production of innovative electric motor concepts," pp. 1–8. IEEE, 12 2020.
[19] N. Simpson, D. J. North, S. M. Collins, and P. H. Mellor, "Additive manufacturing of shaped profile windings for minimal ac loss in electrical machines," *IEEE Transactions on Industry Applications*, vol. 56, pp. 2510–2519, 5 2020.
[20] F. Wu, A. EL-Refaie, and A. Al-Qarni, "Additively manufactured hollow conductors integrated with heat pipes: Design tradeoffs and hardware demonstration," *IEEE Transactions on Industry Applications*, vol. 57, pp. 3632–3642, 7 2021.
[21] P. Melendez-Vega and G. Venkataramanan, "Aluminum foil coils for human scale wind turbines," pp. 1–5. IEEE, 10 2012.
[22] R. Wrobel and P. Mellor, "Design considerations of a direct drive brushless machine with concentrated windings," *IEEE Transactions on Energy Conversion*, vol. 23, pp. 1–8, 3 2008.
[23] P. Arumugam, T. Hamiti, and C. Gerada, "Estimation of eddy current loss in semi-closed slot vertical conductor permanent magnet synchronous machines considering eddy current reaction effect," *IEEE Transactions on Magnetics*, vol. 49, pp. 5326–5335, 2013.
[24] S. Ayat, H. Liu, M. Kulan, and R. Wrobel, "Estimation of equivalent thermal conductivity for electrical windings with high conductor fill factor," pp. 6529–6536. IEEE, 9 2018.
[25] "Applications of anodised aluminium foil." [Online]. Available: https://anofol.de/anwendungen
[26] H. Jordan, "Anodized aluminum foil coil with 538° c capabilities. final report," 11 1980.
[27] D. A. Hewitt, "Approaches to improving thermal performance of inductors with a view to improving power density," 2015.
[28] A. Cai, L. P. Yang, J. P. Chen, T. G. Xi, S. G. Xin, and W. Wu, "Thermal conductivity of anodic alumina film at (220 to 480) k by laser flash technique," *Journal of Chemical and Engineering Data*, vol. 55, pp. 4840–4843, 11 2010.
[29] S. Babicz, S. A. A. Djennad, and G. Velu, "Preliminary study of using anodized aluminum strip for electrical motor windings," pp. 176–179. Institute of Electrical and Electronics Engineers Inc., 12 2014.
[30] L. Reissenweber, A. Stadler, J. v. Lindenfels, and J. Franke, "Improved thermal behavior of an electromagnetic linear actuator with different winding types and the influence on the complex impedance," pp. 1–6. IEEE, 12 2019.
[31] M. Rios, G. Venkataramanan, A. Muetze, and H. Eickhoff, "Thermal performance modeling of foil conductor concentrated windings in electric machines," *IEEE Transactions on Industry Applications*, vol. 54, pp. 4104–4113, 9 2018.
[32] M. Rios and G. Venkataramanan, "Design and construction of a foil winding permanent magnet machine," pp. 2026–2033. IEEE, 10 2020.
[33] F. Ostyn, B. Vanderborght, and G. Crevecoeur, "Design and control of a quasi-direct drive robotic gripper for collision tolerant picking at high speed," *IEEE Robotics and Automation Letters*, pp. 1–8, 2022.
[34] "Igus rebel: Fully integrated single joint." [Online]. Available: https://www.igus.eu/info/rebel-gearbox-system
[35] A. Singh, N. Kashiri, and N. Tsagarakis, "Design of a quasi direct drive actuator for dynamic motions," p. 8516. MDPI, 11 2020.
[36] TQ-Robodrive, "Ilm frameless servo kits," 2020.
[37] A. Husain, "The rise of the 48v robots," 3 2020.
[38] H. Vansompel, P. Sergeant, and L. Dupre, "Optimized design considering the mass influence of an axial flux permanent-magnet synchronous generator with concentrated pole windings," *IEEE Transactions on Magnetics*, vol. 46, pp. 4101–4107, 12 2010.
[39] N. Simpson, R. Wrobel, and P. H. Mellor, "Estimation of equivalent thermal parameters of impregnated electrical windings," *IEEE Transactions on Industry Applications*, vol. 49, pp. 2505–2515, 11 2013.
[40] P. Arumugam, T. Hamiti, and C. Gerada, "Fault tolerant winding design - a compromise between losses and fault tolerant capability," pp. 2559–2565, 2012.
[41] P. Arumugam, T. Hamiti, C. Brunson, and C. Gerada, "Analysis of vertical strip wound fault-tolerant permanent magnet synchronous machines," *IEEE Transactions on Industrial Electronics*, vol. 61, pp. 1158–1168, 3 2014.
[42] F. Franchini, E. Poskovic, L. Ferraris, A. Cavagnino, and G. Bramerdorfer, "Application of new magnetic materials for axial flux machine prototypes," pp. 1–6. IEEE, 5 2017.
[43] R. Wrobel, A. Mlot, and P. H. Mellor, "Contribution of end-winding proximity losses to temperature variation in electromagnetic devices," *IEEE Transactions on Industrial Electronics*, vol. 59, no. 2, pp. 848–857, 2012.
[44] H. Vansompel, A. Yarantseva, P. Sergeant, and G. Crevecoeur, "An inverse thermal modeling approach for thermal parameter and loss identification in an axial flux permanent magnet machine," *IEEE Transactions on Industrial Electronics*, vol. 66, no. 3, pp. 1727–1735, 2019.
[45] D. Neumayr, M. Guacci, D. Bortis, and J. W. Kolar, "New calorimetric power transistor soft-switching loss measurement based on accurate temperature rise monitoring," in *2017 29th International Symposium on Power Semiconductor Devices and IC's (ISPSD)*, pp. 447–450, 2017.

**Jordi Van Damme** (M'18) was born in Gent, Belgium in 1995. He received the Master degree in electromechanical engineering from the University of Ghent, Belgium in 2018. Since then, he has been with the Electrical Energy Laboratory, Ghent University, Belgium where he is currently working towards the Ph.D. degree in electromechanical engineering. In 2019, he was awarded a Ph.D fellowship from the Research Foundation-Flanders (FWO). His current research interests include the design and control of integrated modular electric actuators for mechatronic applications.

**Hendrik Vansompel** was born in Belgium in 1986. He received the MSc and PhD degrees in electromechanical engineering from Ghent University, Ghent, Belgium, in 2009 and 2013, respectively. He is currently a Postdoctoral Research Assistant with the Department of Electromechanical, Systems and Metal Engineering, Ghent University. His research interests include electric machines and power electronics.

**Guillaume Crevecoeur** received the M.Sc. and the Ph.D. degrees in engineering physics from Ghent University, Ghent, Belgium, in 2004 and 2009, respectively. In 2009, he became a Postdoctoral Fellow with the Research Foundation Flanders, Brussels, Belgium, and in 2014, he was appointed as Associate Professor with the Faculty of Engineering and Architecture, Ghent University. He is an active member of Flanders Make, Lommel, Belgium, the strategic research center for the manufacturing industry. His research interests include the modeling, optimization, and control of mechatronic and industrial robotic applications.